JACS
JOURNAL OF THE AMERICAN CHEMICAL SOCIETY
pubs.acs.org/JACS
Article

Impregnating Subnanometer Metallic Nanocatalysts into Self-Pillared Zeolite Nanosheets

Ning Wang, Qiming Sun,* Tianjun Zhang, Alvaro Mayoral, Lin Li, Xue Zhou, Jun Xu, Peng Zhang, and Jihong Yu*

Cite This: https://dx.doi.org/10.1021/jacs.1c00578
Read Online
ACCESS | Metrics & More | Article Recommendations | Supporting Information

ABSTRACT: Impregnation is the most commonly used approach to prepare supported metal catalysts in industry. However, this method suffers from the formation of large metal particles with uneven dispersion, poor thermal stability, and thus unsatisfied catalytic performance. Here, we demonstrate that the self-pillared **MFI** zeolite (silicalite-1 and ZSM-5) nanosheets with larger surface area and abundant Si−OH groups are ideal supports to immobilize ultrasmall monometallic (e.g., Rh and Ru) and various bimetallic clusters via simple incipient wetness impregnation method. The loaded subnanometric metal clusters are uniformly dispersed within sinusoidal five-membered rings of **MFI** and remain stable at high temperatures. The Rh/SP-S-1 is highly efficient in ammonia borane (AB) hydrolysis, showing a TOF value of 430 mol_{H2} mol_{Rh}^{-1} min^{-1} at 298 K, which is more than 6-fold improvement over that of nanosized zeolite-supported Rh catalyst and even comparable with that of zeolite-supported Rh single-atom catalyst. Because of the synergistic effect between bimetallic Rh−Ru clusters and zeolite acidity, the H_2 generation rate from AB hydrolysis over $Rh_{0.8}Ru_{0.2}$/SP-ZSM-5-100 reaches up to 1006 mol_{H2} mol_{metal}^{-1} min^{-1} at 298 K, and also shows record activities in cascade hydrogenation of various nitroarenes by coupling with the hydrolysis of AB. This work demonstrates that zeolite nanosheets are excellent supports to anchor diverse ultrasmall metallic species via the simple impregnation method, and the obtained nanocatalysts can be applied in various industrially important catalytic reactions.

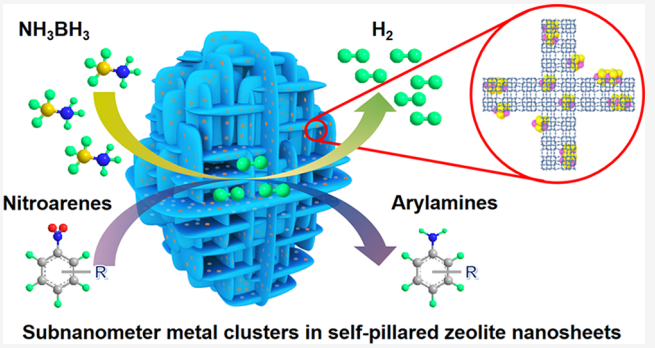

INTRODUCTION

Zeolite-supported metal nanocatalysts have emerged as an indispensable class of industrial catalysts because of their superior catalytic activity and excellent stability, which are widely used in diverse catalytic conversions, such as hydrogenations, dehydrogenations, and reforming reactions.[1−6] The fabrication of ultrasmall metal species is regarded as an effective strategy to improve the catalytic activity and metal utilization, because the small metal species possess high metal dispersion and increased exposure of active sites.[1−3,7,8] Recently, several novel synthetic strategies, such as the ligand-protected method and precursor-stabilization methods have been employed to fabricate zeolite-supported metal catalysts, which exhibit excellent thermal stability and catalytic performance.[9−18] However, most of these synthetic strategies either rely on the use of additional organic templates/ligands or are not universal, which limits their large-scale industrial production. In addition, the obtained zeolite-supported metal catalysts usually suffer from mass transfer limitations in the narrow micropores and the bulky substrate molecules cannot enter microporous channels of zeolites and fail to access active metallic sites, giving unsatisfied universality in different kinds of reactions.[2] In contrast, the impregnation method is one of the most feasible and commonly used approaches to prepare zeolite-supported metal catalysts in industry. However, the impregnation method often leads to the formation of large metal particles with uneven dispersions and severe aggregations during catalytic reactions, showing inferior catalytic activity and stability.[2,19] It is highly desired yet challenging to fabricate zeolite-supported metal catalysts with small metal sizes and superior stability via the impregnation method to meet the requirements of practical industrial applications. Recently, nanosheet-like zeolites have aroused widespread interest due to their high specific surface areas and reduced micropore diffusion length, which exhibit superior catalytic performance and adsorption properties.[20−27] For example, Ryong Ryoo and co-workers synthesized **MFI** zeolite nano-

Received: January 17, 2021

https://dx.doi.org/10.1021/jacs.1c00578
J. Am. Chem. Soc. XXXX, XXX, XXX−XXX

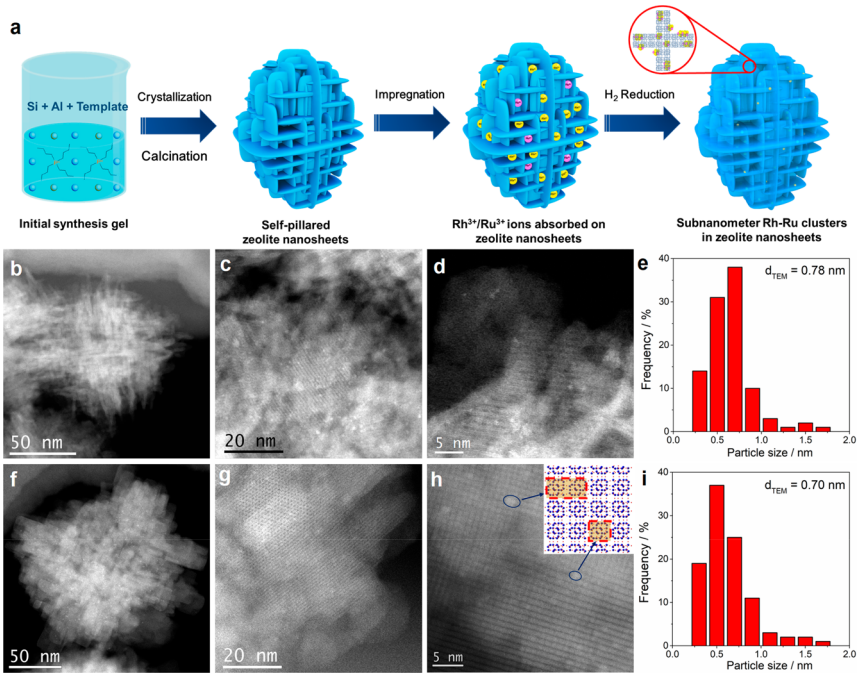

Figure 1. Synthetic procedure and C_s-corrected STEM images of representative self-pillared **MFI** nanosheet-supported metal nanocatalysts. (a) Schematic illustration of the synthetic procedure of subnanometer Rh−Ru clusters in self-pillared **MFI** nanosheets. C_s-corrected STEM images of (b−d) $Rh_{0.8}Ru_{0.2}$/SP-S-1 and (f−h) $Rh_{0.8}Ru_{0.2}$/SP-ZSM-5-100 as well as corresponding size distributions of metal particles of (e) $Rh_{0.8}Ru_{0.2}$/SP-S-1 catalyst and (i) $Rh_{0.8}Ru_{0.2}$/SP-ZSM-5-100. Inset of (h): the schematic model of **MFI** zeolites viewed along [001] orientation. Surface weighted mean cluster diameter $d_{TEM} = \Sigma n_i d_i^3/\Sigma n_i d_i^2$, where n_i is the number of metallic clusters having diameter d_i.

sheets with a 2 nm thickness by using a bifunctional diquaternary ammonium-type surfactant, which exhibited remarkably improved activity of the conversion of large organic molecules and prolonged lifetime in methanol-to-gasoline conversions as compared with conventional **MFI** zeolites.[22] Michael Tsapatsis and co-workers reported the synthesis of self-pillared zeolite nanosheets by using relatively inexpensive tetrabutylphosphonium hydroxide as a template.[20] The tetrabutylphosphonium ions act as structure-directing groups are incorporated intact in the zeolite framework, and contribute to the anisotropic growth and the 90° rotational intergrowths of the **MFI** framework, giving rise to self-pillared zeolites composed of orthogonally connected single−unit cell lamellae. The zeolite nanosheets show superior catalytic efficiency for the etherification of bulky substrates. In addition, compared with conventional zeolite crystals, the ultrathin zeolite nanosheets possess significantly increased external surface area and abundant Si−OH defects, which will facilitate the dispersion of metal precursors in zeolites and the formation of ultrafine metal species after the reduction process. The zeolite nanosheet-supported metal catalysts can be expected to possess excellent catalytic performance by integrating ultrasmall and ultrastable metal species with remarkably enhanced mass transport efficiency of ultrathin zeolites for reactants and products during catalytic reactions.

Herein, we employed self-pillared **MFI** zeolite nanosheets (SP-S-1 and SP-ZSM-5) as efficient supports to immobilize a series of ultrasmall monometallic (Rh and Ru) and bimetallic clusters (Rh−Ru, Rh−Au, Rh−Ni, Rh−Co, Rh−Fe, Rh−Mn, Rh−Cu, Rh−Zn, Ru−Cu, Ru−Fe, and Ru−Ni) via a simple incipient wetness impregnation method. Extended X-ray absorption fine structure (EXAFS) analyses and C_s-corrected scanning transmission electron microscopy (STEM) confirm that the metal clusters are subnanometer in size and uniformly distributed throughout zeolite nanosheets, and most of the metal clusters are confined within the sinusoidal five-membered rings of zeolite nanosheets. Compared with nanosized zeolite-supported metal catalysts, the self-pillared zeolite nanosheet-immobilized metal catalysts possess remarkably improved thermal stability at various redox atmospheres at 600 °C. The obtained zeolite nanosheet-supported metal catalysts are applied in ammonia borane (AB, NH_3BH_3) hydrolysis, which is regarded as one of the most promising liquid-phase chemical hydrogen storage methods.[28−31] The Rh/SP-S-1 exhibits an excellent H_2 generation rate (430 min^{-1}) from AB hydrolysis at 298 K, which is more than 6-fold improvement than that over nanosized zeolite-supported Rh catalyst (Rh/Nano S-1, 66 min^{-1}), and even comparable with that over the single Rh atom catalyst (Rh_1@S-1, 499 min^{-1}). The excellent catalytic activity of Rh/SP-S-1 can be mainly attributed to the remarkably improved hydrophilicity and transport efficiency. In addition, thanks to the synergistic effect between bimetallic Rh−Ru clusters and Brønsted acid sites of zeolites, the optimized $Rh_{0.8}Ru_{0.2}$/SP-ZSM-5-100 exhibits a superior H_2 generation rate from AB hydrolysis, affording a superhigh turnover frequency (TOF) of 1006 min^{-1} at 298 K, which represents the top activity among all of the best heterogeneous catalysts under similar conditions. Isotopic experiments reveal that both acidities of zeolites and bimetallic Rh−Ru synergy can promote the activation of water, which remarkably accelerates the H_2 evolution rate from the hydrolysis of AB. In addition, the $Rh_{0.8}Ru_{0.2}$/SP-ZSM-5-100 also exhibits record activities in cascade hydrogenation of various nitroarenes by coupling with the hydrolysis of AB at room temperature.

https://dx.doi.org/10.1021/jacs.1c00578
J. Am. Chem. Soc. XXXX, XXX, XXX−XXX

RESULTS AND DISCUSSION

Synthesis and Characterization of Catalysts. Figure 1a shows the schematic illustration of the synthetic procedure of metallic subnanometer clusters in self-pillared **MFI** nanosheets taking Rh−Ru as representative examples. The self-pillared silicalite-1 (SP-S-1) and ZSM-5 (SP-ZSM-5) nanosheets are first synthesized by using tetrabutyl phosphorus hydroxide (TBPOH) as the template with molar compositions of SiO_2:0.3TBPOH:yAl_2O_3:zNaOH:10H_2O:4EtOH (y = 0, 0.0025, and 0.005; z = 0, 0.005, and 0.0125) under hydrothermal conditions at 115 °C for 2 days.[20] Following this, the organic templates and Na ions are removed by calcination in air and ion-exchange with NH_4NO_3. Finally, various Rh_xRu_{1-x} (x = 1.0, 0.8, 0.6, 0.4, 0.2, and 0) clusters are immobilized in **MFI** zeolite nanosheets by impregnating different amounts of the $RhCl_3$ and $RuCl_3$ solution in zeolites followed by H_2 reduction at 400 °C. The obtained catalysts are named as Rh_xRu_{1-x}/SP-S-1, Rh_xRu_{1-x}/SP-ZSM-5−200, and Rh_xRu_{1-x}/SP-ZSM-5-100, in which the 200 and 100 represent the Si/Al ratio in initial synthesis gels. In comparison, the Rh/Nano S-1 is also prepared by the same incipient wetness impregnation method as the Rh/SP-S-1 except for replacing the self-pillared S-1 nanosheets with conventional S-1 nanocrystals that synthesized by using tetrapropylammonium hydroxide (TPAOH) as the template with a molar composition of SiO_2:TPAOH:H_2O = 1:0.4:35.

The powder X-ray diffraction (XRD) patterns of Rh_xRu_{1-x}/SP-S-1, Rh_xRu_{1-x}/SP-ZSM-5, and Rh/Nano S-1 all exhibit typical diffraction peaks corresponding to the **MFI** framework (Figures S1 and S2 and Figure 2a). The diffraction peaks of Rh_xRu_{1-x}/SP-S-1 and Rh_xRu_{1-x}/SP-ZSM-5 are widened

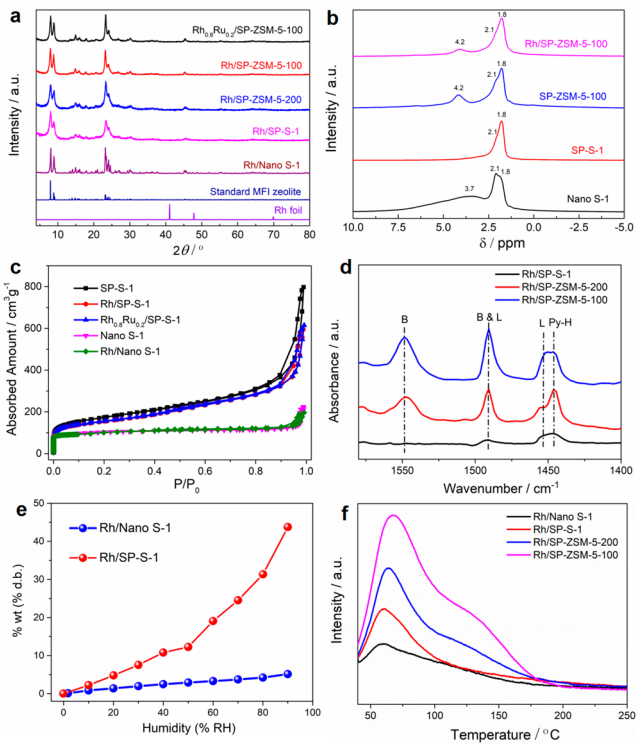

Figure 2. Characterizations of various catalysts. (a) XRD patterns of representative samples as well as standard MFI zeolite and Rh foil. (b) ^{1}H MAS NMR spectra, (c) N_2 adsorption/desorption isotherms, (d) in situ infrared spectra of the adsorbed pyridine at 350 °C, (e) water adsorption isotherms, and (f) H_2O-TPD curves of various catalysts.

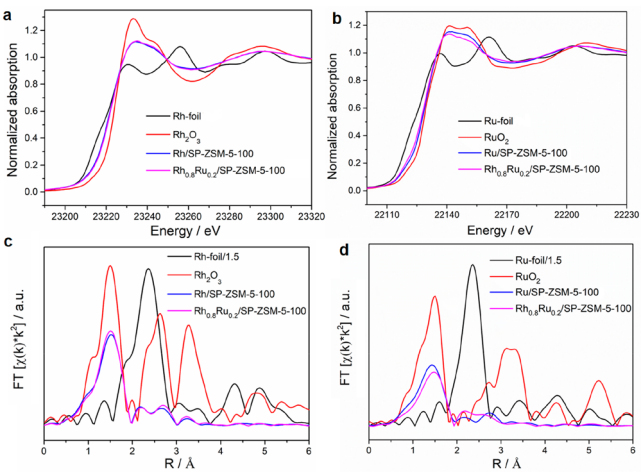

Figure 3. XANES and EXAFS measurements of various samples and corresponding standards. (a) Rh K-edge XANES spectra of Rh foil, Rh_2O_3, Rh/SP-ZSM-5-100, and $Rh_{0.8}Ru_{0.2}$/SP-ZSM-5-100. (b) Ru K-edge XANES spectra of Ru foil, RuO_2, Ru/SP-ZSM-5-100, and $Rh_{0.8}Ru_{0.2}$/SP-ZSM-5-100. Fourier transform of k^2-weighted EXAFS spectra of (c) Rh foil, Rh_2O_3, Rh/SP-ZSM-5-100, and $Rh_{0.8}Ru_{0.2}$/SP-ZSM-5-100 at Rh K-edge, and (d) Ru foil, RuO_2, Ru/SP-ZSM-5-100, and $Rh_{0.8}Ru_{0.2}$/SP-ZSM-5-100 at Ru K-edge.

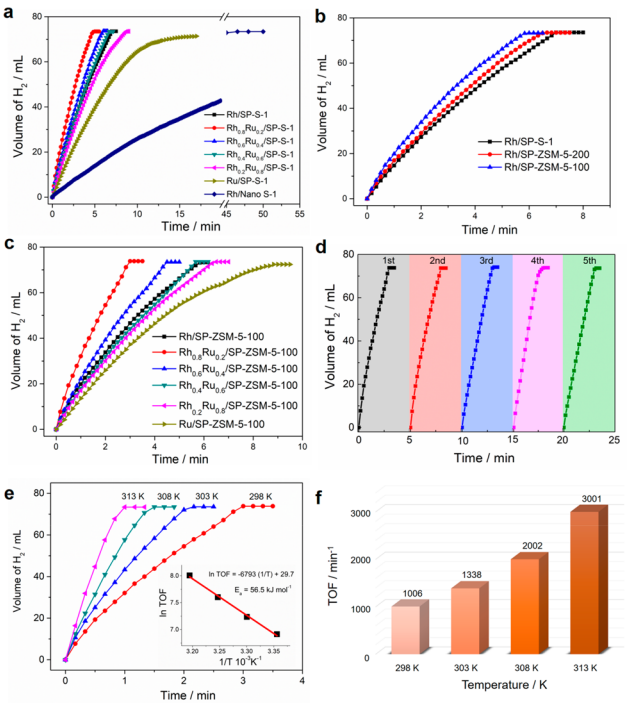

Figure 4. Catalytic activity of H_2 generation from AB hydrolysis over various catalysts. Volume of the H_2 generated from AB (1 M) hydrolysis versus time at 298 K (n_{Metal}/n_{AB} = 0.001) catalyzed by (a) Rh/Nano S-1 Rh/SP-S-1, Ru/SP-S-1, and various Rh_xRu_{1-x}/SP-S-1 catalysts, (b) Rh/SP-S-1, Rh/SP-ZSM-5-200, and Rh/SP-ZSM-5-100 catalysts, and (c) Rh/SP-ZSM-5-100, Ru/SP-ZSM-5-100, and various Rh_xRu_{1-x}/SP-ZSM-5-100 catalysts. (d) The recycling tests of AB hydrolysis over $Rh_{0.8}Ru_{0.2}$/SP-ZSM-5-100 catalyst at 298 K. (e) Volume of the H_2 generated from AB (1 M) hydrolysis versus time at various temperatures over $Rh_{0.8}Ru_{0.2}$/SP-ZSM-5-100 catalyst and (f) corresponding TOF values (n_{Metal}/n_{AB} = 0.001). Inset of e: Arrhenius plot (ln TOF versus 1/T).

https://dx.doi.org/10.1021/jacs.1c00578
J. Am. Chem. Soc. XXXX, XXX, XXX−XXX

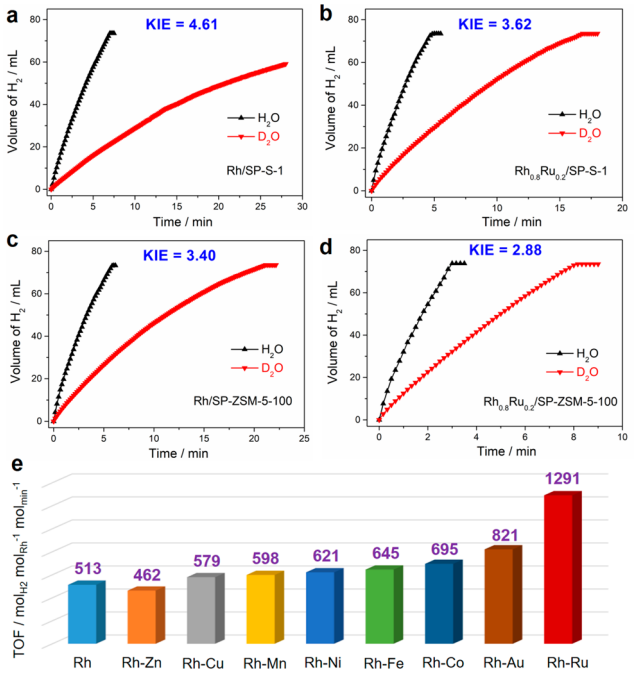

Figure 5. Kinetic isotope measurements and catalytic activity of H_2 generation from AB hydrolysis over various self-pillared ZSM-5-100-supported Rh-based nanocatalysts. The volume of the H_2 generated from AB (1 M) hydrolysis versus time using H_2O and D_2O as the reactants at 298 K over (a) Rh/SP-S-1, (b) $Rh_{0.8}Ru_{0.2}$/SP-S-1, (c) Rh/SP-ZSM-5-100, and (d) $Rh_{0.8}Ru_{0.2}$/SP-ZSM-5-100 catalysts. (e) TOF values of various self-pillared ZSM-5-100-supported Rh-based nanocatalysts.

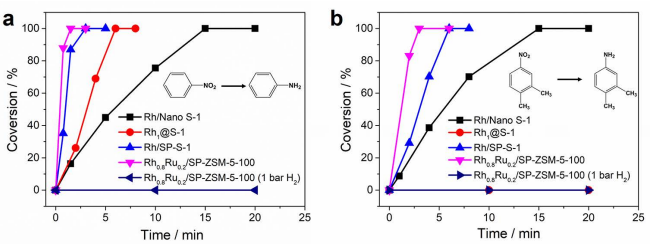

Figure 6. Catalytic activity of the cascade hydrogenation of nitrobenzene and 4-nitroxylene coupling with the hydrolysis of AB over various catalysts. (a) Cascade hydrogenation of nitrobenzene (b) Cascade hydrogenation of 4-nitroxylene coupling with AB hydrolysis over various catalysts. Reaction condition: 0.2 mmol of nitrobenzene or 4-nitroxylene, 1 mmol of NH_3BH_3, the ratio of Rh/substrate is 0.0025, MeOH/H_2O = 8 mL/12 mL, 298 K. The $Rh_{0.8}Ru_{0.2}$/SP-ZSM-5-100 (1 bar H_2) are tested under the same condition with others just replacing NH_3BH_3 by 1 bar of H_2.

compared to that of Rh/Nano S-1, which is attributed to the formation of smaller zeolite crystals. No diffraction peaks of metallic Rh and Ru (foils) are detected in samples because of the relatively low metal loadings, small size, and uniform metal dispersions. On the basis of the inductively coupled plasma (ICP) atomic emission spectroscopy measurements, the molar ratios of Si/Al of SP-ZSM-5-200 and SP-ZSM-5-100 are 253 and 75, respectively. The loading amount of P element in SP-S-1, SP-ZSM-5-200, and SP-ZSM-5-100 are 1.26, 1.22, and 1.12 wt %, respectively, because of the formation of a small amount of P_2O_5 after calcination of templates in air. All metal-containing samples possess similar metal loading amounts of 0.42−0.44 wt % (Table S1) and the molar ratios of Rh/Ru in $Rh_{0.8}Ru_{0.2}$/SP-S-1, $Rh_{0.6}Ru_{0.4}$/SP-S-1, $Rh_{0.4}Ru_{0.6}$/SP-S-1, and $Rh_{0.2}Ru_{0.8}$/SP-S-1 are 0.81/0.19, 0.62/0.38, 0.39/0.61, and 0.19/0.81, respectively. The molar ratios of Rh/Ru in Rh_xRu_{1-x}/SP-ZSM-5-100 are also consistent with the predesigned values (Table S1).

Figure S3 shows the TEM images of pure SP-S-1, SP-ZSM-5-200, and SP-ZSM-5-100 zeolites. All of these zeolites exhibit self-pillared nanosheet-like morphology and the thickness of each lamellae in SP-S-1 and SP-ZSM-5-200 are only 2−3 nm. The introduction of more Al atoms into zeolite frameworks can slightly enlarge the zeolite crystals, but the average thickness of zeolites in SP-ZSM-5-100 is only about 10 nm. In comparison, the conventional S-1 nanocrystals exhibit a morphology of hexagonal prism with dimensions of 100−200 nm. The high-resolution TEM and C_s-corrected high angle annular dark field STEM (HAADF-STEM) images of representative samples are shown in Figure S4 and Figure 1b−i. The introduction of metal species does not change the nanosheet-like morphology of zeolites. Significantly, most of the metal species are confined within micropores of self-pillared **MFI** nanosheets and more than 80% of metal species are less than 1 nm in size. The average metal sizes of $Rh_{0.8}Ru_{0.2}$/SP-S-1 and $Rh_{0.8}Ru_{0.2}$/SP-ZSM-5-100 are as low as 0.78 and 0.70 nm, respectively, and the ultrasmall metal clusters are uniformly immobilized throughout the zeolite nanosheets with superhigh dispersions and narrow size distributions. By looking at the zeolite along with the [001] projection, based on the C_s-corrected STEM analyses and the schematic crystallographic representation along this zone axis (Figure 1h inset); most of the metal clusters are confined within one or several "rectangular units" which are formed by the sinusoidal five-membered rings. In contrast, the metal nanoparticles (NPs) supported onto S-1 nanocrystals are quite large (~4 nm) with uneven distributions and substantially all of the metal NPs are located on the outside of zeolite nanocrystals (Figure S4f1−f3). H_2-chemisorption measurements reveal that the metal dispersions of Rh/SP-S-1, Rh/SP-ZSM-5-100, and $Rh_{0.8}Ru_{0.2}$/SP-ZSM-5-100 are 83.4, 86.1, and 84.4%, respectively, which are much higher than that of Rh/Nano S-1 (23.0%) (Figure S5). The above results indicate that compared with conventional zeolite nanocrystals, the ultrathin zeolite nanosheets are much beneficial for improving the dispersion of metal precursors and forming ultrafine metal clusters upon reduction process. Scanning electron microscopy (SEM) exhibits that many large Rh particles are located on the outside of zeolites in Rh/Nano S-1, but they are hardly observed in Rh/SP-S-1, Rh/SP-ZSM-5-100, and $Rh_{0.8}Ru_{0.2}$/SP-ZSM-5-100 (Figure S6). The chemical elemental mappings for Si, O, Al, Rh, and Ru elements of $Rh_{0.8}Ru_{0.2}$/SP-ZSM-5-100 are shown in Figure S7. The Rh and Ru are uniformly distributed throughout the SP-ZSM-5 crystals in a similar position, demonstrating the formation of a bimetallic system.

The ^1H and ^{29}Si MAS NMR spectra of samples are shown in Figure 2b and Figures S8 and S9. In the ^1H MAS NMR spectra, the signals at 1.8−2.1 and 3.7 ppm can be attributed to isolated Si−OH and H-bonded Si−OH, respectively.[32] Notably, compared with the Nano S-1, the SP-S-1, SP-ZSM-5-100, and Rh/SP-ZSM-5-100 possess more isolated Si−OH defects, and the introduction of metal species leads to some decreases in isolated Si−OH sites of zeolites. On the basis of the above results, we can deduce that the isolated Si−OH defects are probably responsible for immobilizing metal clusters, and the metal dispersions and sizes become better

https://dx.doi.org/10.1021/jacs.1c00578
J. Am. Chem. Soc. XXXX, XXX, XXX−XXX

Table 1. Catalytic Results for the Cascade Hydrogenation of Nitroarenes by Coupling with the Hydrolysis of AB over Various Catalysts

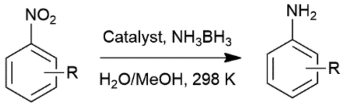

Entry	Catalysts	Substrate	Product	Time /min	Con/Sel[c] /%	Ativty/[d] $mol_{Arylamine}\ mol_{metal}^{-1}\ min^{-1}$
1	$Rh_{0.8}Ru_{0.2}$/SP-ZSM-5-100[a]	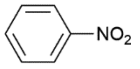	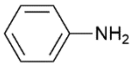	1.5	100/>99	267
	Rh/SP-S-1[a]			3	100/>99	133
	Rh/Nano S-1[a]			15	100/>99	26.7
	Rh_1@S-1[a]			6	100/>99	66.7
	$Rh_{0.8}Ru_{0.2}$/SP-ZSM-5-100[b]			20	Trace	0
2[a]	$Rh_{0.8}Ru_{0.2}$/SP-ZSM-5-100[a]	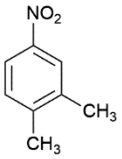	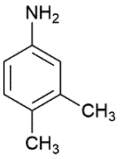	3	100/>99	133
	Rh/SP-S-1[a]			6	100/>99	100
	Rh/Nano S-1[a]			15	100/>99	26.7
	Rh_1@S-1[a]			20	Trace	0
	$Rh_{0.8}Ru_{0.2}$/SP-ZSM-5-100[b]			20	Trace	0
3	$Rh_{0.8}Ru_{0.2}$/SP-ZSM-5-100[a]	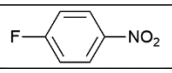	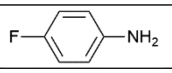	3	100/>99	133
4	$Rh_{0.8}Ru_{0.2}$/SP-ZSM-5-100[a]	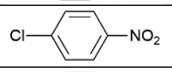	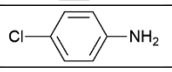	3	100/>99	133
5	$Rh_{0.8}Ru_{0.2}$/SP-ZSM-5-100[a]	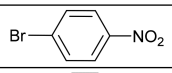	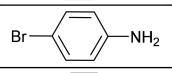	3	100/>99	133
6	$Rh_{0.8}Ru_{0.2}$/SP-ZSM-5-100[a]	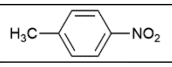	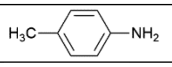	1.5	100/>99	267
7	$Rh_{0.8}Ru_{0.2}$/SP-ZSM-5-100[a]	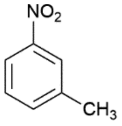	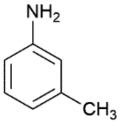	3	100/>99	133
8	$Rh_{0.8}Ru_{0.2}$/SP-ZSM-5-100[a]	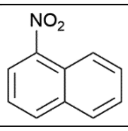	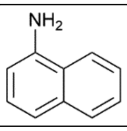	3	100/>99	133

[a]Reaction condition: 0.2 mmol of nitro compound, 1 mmol of NH_3BH_3, the Rh/substrate ratio is 0.0025, MeOH/H_2O = 8 mL/12 mL at 298 K. [b]Replacing NH_3BH_3 by 1 bar of H_2. [c]All products were analyzed by gas chromatography−mass spectrometry. [d]The activity was calculated based on the total amount of metal atoms in catalysts when the conversion of nitroarenes reached 100%.

and smaller with the increase of isolated Si−OH defects in zeolites. The peak at 4.2 ppm ascribed to bridging OH groups (SiOHAl) is observable in SP-ZSM-5-100 and Rh/SP-ZSM-5-100, indicating the presence of Brønsted acid sites.[33] In the ^{29}Si MAS NMR spectra, the peaks at −110 to −115 ppm are the predominant signal in all samples corresponding to Si(4Si) species, and the SP-S-1 possesses more Si(3Si1OH) species than the Nano S-1, indicating the formation of more defect sites.

To identify the atomic structure and electronic property of metal species, we measured the X-ray absorption near edge structure (XANES) and extended X-ray absorption fine structure (EXAFS) of Rh/SP-ZSM-5-100, Ru/SP-ZSM-5-100, and $Rh_{0.8}Ru_{0.2}$/SP-ZSM-5-100 (Figures 3 and Figures S10, Table S2). Notably, Rh/SP-ZSM-5-100 and $Rh_{0.8}Ru_{0.2}$/SP-ZSM-5-100 possess a more intense white line (i.e., the first prominent peak following the absorption edge) in Rh K-edge XANES spectra than that of Rh foil, suggesting the oxidized state of Rh in these two samples. Such phenomenon can be attributed to the formation of ultrasmall metal clusters and the interaction between metal clusters and skeleton oxygen atoms of zeolites. Similarly, the XANES spectra of Ru/SP-ZSM-5-100 and $Rh_{0.8}Ru_{0.2}$/SP-ZSM-5-100 at Ru K-edge (Figure 3b) also exhibit some differences from the Ru foil. Notably, at the Ru K-edge XANES spectra, the intensity of the white line at 22140 eV of $Rh_{0.8}Ru_{0.2}$/SP-ZSM-5-100 is lower than that of Ru/SP-ZSM-5-100, and the $Rh_{0.8}Ru_{0.2}$/SP-ZSM-5-100 also exhibits a shift to lower binding energy as compared with Ru/SP-ZSM-5-100. However, compared with Rh/SP-ZSM-5-100, the opposite trend in the intensity of the white line at 23235 eV and binding energy appeared in $Rh_{0.8}Ru_{0.2}$/SP-ZSM-5-100 at the Rh K-edge XANES spectra. All the above changes in the XANES demonstrate that electrons are transferred from Rh to Ru in $Rh_{0.8}Ru_{0.2}$/SP-ZSM-5-100, indicating the formation of a bimetallic Rh−Ru structure.[34] According to the EXAFS results, the average coordination numbers (CNs) of Rh−O with a bond length of about 2.02 Å for $Rh_{0.8}Ru_{0.2}$/SP-ZSM-5-100 is 3.6, which is slightly higher than that of Rh/SP-ZSM-5-100

https://dx.doi.org/10.1021/jacs.1c00578
J. Am. Chem. Soc. XXXX, XXX, XXX−XXX

(CN = 3.4), Figure 3c. In contrast, the CN of Ru−O with a bond length of about 2.00 Å for $Rh_{0.8}Ru_{0.2}$/SP-ZSM-5-100 is lower than that of Ru/SP-ZSM-5-100 (3.4 vs 4.1), Figure 3d. These results further indicate that compared to monometallic counterparts, the bimetal Rh−Ru clusters in $Rh_{0.8}Ru_{0.2}$/SP-ZSM-5-100 are electron-rich (Ru) and electron-poor (Rh) metal sites, respectively. Notably, all of the CNs of metal−metal (e.g., Rh−Rh, Ru−Rh, and Ru−Ru) bonds in Rh/SP-ZSM-5-100, Ru/SP-ZSM-5-100, and $Rh_{0.8}Ru_{0.2}$/SP-ZSM-5-100 are less than 2. These low CNs show that the obtained metal clusters are composed of a small number of atoms and possess subnanometer dimensions, which is consistent with the observation of C_s-corrected STEM images. The X-ray photoelectron spectroscopy (XPS) measurements were also performed to determine the electronic states of metal species in samples. The peaks at 307.8 and 312.5 eV corresponding to the Rh $3d_{5/2}$ and Rh $3d_{3/2}$ of Rh(0) can be observed in Rh/SP-ZSM-5-100 (Figure S11).[35] By comparison, the corresponding peaks slightly shift to the higher binding energy of 308.1 and 312.8 eV in $Rh_{0.8}Ru_{0.2}$/SP-ZSM-5-100, which indicates that the Rh species in $Rh_{0.8}Ru_{0.2}$/SP-ZSM-5-100 is more electron-poor than that in Rh/SP-ZSM-5-100, in accordance with XANES results.

N_2 adsorption/desorption measurements show that the specific surface areas of the SP-S-1 and SP-ZSM-5-100 are 608 and 567 m^2/g, which is much higher than that of Nano S-1 (375 m^2/g) (Figure 2 c and Figure S12, Table S1). It can be mainly attributed to the formation of ultrathin zeolite nanosheets in the SP-S-1 and SP-ZSM-5-100, possessing significantly increased external surface areas. The large specific surface area of self-pillared zeolite nanosheets is also a very important factor in the formation of ultrafine metal clusters with high dispersions. Compared to the pure SP-S-1 and SP-ZSM-5-100 zeolites, a decrease in micropore volume (0.007−0.008 cm^3/g) can be observed for metal/SP-S-1 and metal/SP-ZSM-5-100, attributed to the partial occupation of zeolite micropores by the metal clusters. However, more than 90% of void spaces (>0.075 cm^3/g microporous volumes and >507 m^2/g surface areas) are reserved in self-pillared MFI nanosheet-supported metal samples. In contrast, the microporous volumes of Rh/Nano S-1 and pure Nano S-1 are identical, which indicates that almost all of the metal nanoparticles are likely located on the outer surface of Nano S-1 rather than the inside of the zeolite matrix, in accordance with the observation of TEM images.

The ammonia temperature-programmed desorption (NH_3-TPD) measurements are employed to evaluate the acidity of samples. As shown in Figure S13, the Rh/Nano S-1 shows no acidity, whereas a peak at about 160 °C can be observed in Rh/SP-S-1, which can be mainly attributed to the existence of the P_2O_5 in the sample. With the introduction of Al into zeolite frameworks, a peak at 350−400 °C can be observed in the Rh/SP-ZSM-5-200 and Rh/SP-ZSM-5-100, indicating the generation of strong acid sites. Among all of the samples, the Rh/SP-ZSM-5-100 exhibited the highest acid concentration and strength because of its lowest Si/Al ratio. In situ infrared (IR) spectroscopy of the adsorbed pyridine at different temperatures was also used to probe the acidity of samples. As shown in Figure 2d and Figure S14, the bands at 1455 and 1545 cm^{-1} are assigned to the Lewis and Brønsted acid sites, respectively.[36,37] The numbers of Lewis acid sites of Rh/SP-S-1, Rh/SP-ZSM-5−200, and Rh/SP-ZSM-5-100 are 6.1, 17.6, and 17.8 μmol/g at 350 °C, respectively. Among all samples, the Rh/SP-ZSM-5-100 possesses the highest number of Brønsted acid sites up to 56.0 μmol/g at 350 °C, which is over 2-fold higher than that of Rh/SP-ZSM-5−200 (24.8 μmol/g). In contrast, there are no Brønsted acid sites in Rh/SP-S-1 (Table S3). The hydrophilicity of samples is determined by water absorption measurement. As shown in Figure 2e, the water absorption of the Rh/SP-S-1 sample is as high as 43.8 wt %, more than 8 times higher than that of Rh/Nano S-1 (5.1 wt %), suggesting Rh/SP-S-1 is much more hydrophilic than Rh/Nano S-1, which can be attributed to its ultrathin nanosheet-like morphology and the existence of more defects in the SP-S-1 nanosheets. The H_2O-TPD measurements further reveal that the Rh/SP-S-1 and Rh/SP-ZSM-5 possess stronger chemisorption for water than does Rh/Nano S-1, and among all of the samples, the Rh/SP-ZSM-5-100 exhibits the strongest chemisorption for water (Figure 2f).

The thermal stability of representative $Rh_{0.8}Ru_{0.2}$/SP-ZSM-5-100 is also investigated in various atmospheres. The average sizes of Rh−Ru species are only 1.1, 0.95, and 1.2 nm after thermal treatment at 600 °C under H_2, N_2, and O_2−H_2 cycle atmospheres, respectively (Figures S15−S17). In contrast, the metal sizes of Rh/Nano S-1 are dramatically increased to 4.5−8.5 nm after calcination under these atmospheres. It indicates that the self-pillared zeolite nanosheet-immobilized subnanometer metallic clusters possess significantly improved thermal stability than conventional nanosized zeolite-supported metal catalysts. Most significantly, besides Rh−Ru clusters, the SP-ZSM-5-100 can be also used as powerful supports to immobilize various ultrafine metal clusters. As shown in Figures S18−S27, a series of metal clusters, such as Rh−Au, Rh−Ni, Rh−Co, Rh−Fe, Rh−Mn, Rh−Cu, Rh−Zn, Ru−Cu, Ru−Fe, and Ru−Ni with subnanometric sizes and superhigh dispersions are successfully immobilized into SP-ZSM-5-100 nanosheets via the incipient wetness impregnation method.

Catalytic Activity of Hydrogen Generation from AB Hydrolysis. We demonstrate the catalytic efficiency of various self-pillared zeolite nanosheet-supported metal nanocatalysts for the H_2 generation from AB hydrolysis. As in Figure 4a, the H_2 generation rate from AB hydrolysis over Rh/SP-S-1 reaches up to 430 mol_{H2} mol_{Rh}^{-1} min^{-1} at 298 K, which is 6-fold higher than that of Rh/Nano S-1 (66 mol_{H2} mol_{Rh}^{-1} min^{-1}). Notably, such a value is also comparable with that of Nano S-1-encaged single Rh atom (Rh_1@S-1) (499 mol_{H2} mol_{metal}^{-1} min^{-1}) under the same catalytic condition,[13] although the Rh clusters in Rh/SP-S-1 are larger than single Rh atoms. The excellent catalytic activity can be mainly attributed to the superior hydrophilicity and enhanced mass transport efficiency of reactants and products among zeolite nanosheets. Significantly, the introduction of a suitable amount of Ru into Rh species to form Rh−Ru bimetallic clusters could further enhance the catalytic performance for AB hydrolysis. Among all of the bimetallic catalysts, the optimized $Rh_{0.8}Ru_{0.2}$/SP-S-1 exhibits the highest H_2 generation rate from AB hydrolysis, affording a TOF value of 620 mol_{H2} mol_{metal}^{-1} min^{-1}. In addition, the H_2 generation rates over the Rh/SP-ZSM-5 are further improved than that over the Rh/SP-S-1, and the H_2 generation rates are improved gradually with the increase in zeolite acidity (Figure 4b and Figure S28, Table S4). The catalytic activities of AB hydrolysis are further tested over Rh/SP-SZM-5-100, Ru/SP-SZM-5-100, and various Rh_xRu_{1-x}/SP-ZSM-5-100 catalysts at 298 K (Figure 4c). Among all of the catalysts, the $Rh_{0.8}Ru_{0.2}$/SP-SZM-5-100 catalyst exhibits the best catalytic performance: 73.5 mL of

https://dx.doi.org/10.1021/jacs.1c00578
J. Am. Chem. Soc. XXXX, XXX, XXX−XXX

stoichiometric H_2 (H_2/AB = 3) can be released within 3.0 min (n_{metal}/n_{AB} = 0.001) toward 100% decomposition of AB, affording a superhigh TOF value of 1006 mol_{H2} mol_{metal}^{-1} min^{-1} at 298 K. Such a TOF value is more than 15-fold improvement compared to that of the Rh/Nano S-1, which is also much higher than that of most state-of-the-art heterogeneous catalysts (Table S5).[13,38−40] The activities of AB hydrolysis over bare SP-S-1 and SP-ZSM-5 zeolites are also investigated at 298 K. H_2 (0.55 mL) is released in 10 min over bare SP-ZSM-5 zeolite, which is about 2-fold higher than that over bare SP-S-1 (0.28 mL), indicating that the Brønsted acid site of zeolite benefits for the hydrolysis of AB (Figure S29). However, compared with metal-containing zeolite catalysts, the H_2 generation over pure zeolites is almost negligible, indicating that the H_2 generation from AB hydrolysis over zeolite-supported metal catalysts mainly relies on the introduction of metal species. Notably, the TOF ratio of $Rh_{0.8}Ru_{0.2}$/SP-ZSM-5-100 to Rh/SP-ZSM-5-100 is 1.96, which is higher than that of $Rh_{0.8}Ru_{0.2}$/SP-S-1 to Rh/SP-S-1 (1.44). Considering the similar metal size of these catalysts, the above results indicate that the synergistic effect between bimetallic clusters and acidic zeolites is more conducive to accelerate the H_2 generation rate from AB hydrolysis. According to the gas chromatography analysis and ^1H NMR and ^{11}B NMR measurements, the gaseous H_2, as well as NH_4^+ and BO_2^- ions, are the final products after AB hydrolysis over catalysts (Figures S30−32). The AB hydrolysis follows the equation as below:

$$NH_3BH_3 + 2H_2O \xrightarrow{\text{catalyst}} NH_4^+ + BO_2^- + 3H_2\uparrow$$

The $Rh_{0.8}Ru_{0.2}$/SP-SZM-5-100 exhibits excellent recycling stabilities during AB hydrolysis. After the completion of the previous run, the catalyst is isolated from the reaction solution and washed by dilute HCl solution (0.1 M). After successive five cycles, the H_2 generation rates over $Rh_{0.8}Ru_{0.2}$/SP-SZM-5-100 keep unchanged (Figure 4d). Significantly, the size of metal clusters, morphology and crystallinity of zeolites, and metal loadings of spent catalysts remain identical with the fresh one based on the TEM, XRD, and ICP measurements (Figures S33 and S34, Table S1). Moreover, the durability tests are also investigated over the $Rh_{0.8}Ru_{0.2}$/SP-SZM-5-100. Upon completion of the previous run of the AB hydrolysis, another equivalent of AB (2 M, 0.5 mL) is directly added into the reaction system to examine the activity of AB hydrolysis. As shown in Figure S35a, 73.5 mL of stoichiometric H_2 (H_2/AB = 3) can be released in each run, and a high TOF value of 812 min^{-1} is achieved even after consecutive five injections of AB solution. The slightly decreased catalytic activity after several consecutive injections of AB solution is mainly attributed to the increased viscosity of the solution and the deactivation effect of the increasing metaborate concentration during the hydrolysis reaction.[41] Note that the activity of the spent catalyst after consecutive five injections of AB solution can be recovered by isolated from the reaction solution and washed by dilute HCl solution (Figure S35b). The above results further reveal excellent durable and recycling stability of self-pillared zeolite-supported metal catalysts in the AB hydrolysis reactions. Moreover, the H_2 generation rates accelerate along with the reaction temperatures, and the TOF value of $Rh_{0.8}Ru_{0.2}$/SP-SZM-5-100 is as high as 3001 mol_{H2} mol_{metal}^{-1} min^{-1} at 313 K, with an apparent activation energy of 56.5 kJ mol^{-1} (Figure 4e, f).

The kinetic studies of AB hydrolysis are also investigated over the $Rh_{0.8}Ru_{0.2}$/SP-SZM-5-100. The H_2 generation rates over the $Rh_{0.8}Ru_{0.2}$/SP-SZM-5-100 almost keep unchanged with the increase of AB concentrations from 0.5 to 2 M, but gradually accelerate with the increase of catalyst concentrations (Figures S36 and S37a). The logarithmic plots of H_2 generation rates versus catalyst concentrations exhibited a slope of 1.274 (Figure S37b), indicating the first-order kinetics with respect to the catalyst concentration. To further investigate the mechanistic insights of AB hydrolysis, the isotopic experiments using D_2O instead of H_2O as the reactant are also carried out over various catalysts. As shown in Figures 5a−d, compared with H_2O as the reactant, all of the catalysts show much slower H_2 generation rates when the D_2O is used as the reactant. Based on previous literature, the kinetic isotope effect (KIE) value is calculated as the ratio of rate constants between H_2O and D_2O as the reactants, which is regarded as an effective method to determine whether the cleavage of the O−H bond is the rate-determining step during the AB hydrolysis.[42−44] The KIE values of $Rh_{0.8}Ru_{0.2}$/SP-S-1 and Rh/SP-ZSM-5-100 are 3.62 and 3.40, respectively, which are lower than that of Rh/SP-S-1 (KIE = 4.61). The above results demonstrate that the activation of the water molecule or the cleavage of the O−H bond is the rate-determining step for AB hydrolysis and both of the bimetallic Rh−Ru synergy and acidic sites of zeolites can promote the activation of the water molecule. Notably, among all of the catalysts, the $Rh_{0.8}Ru_{0.2}$/SP-ZSM-5-100 catalyst exhibits the lowest KIE value of 2.88, suggesting its strongest ability to active water molecules.

The above results further indicate that the establishment of efficient synergy by coupling bimetallic clusters with Bronsted acid sites of zeolites can remarkably contribute to the activation of water molecules and boost the efficiency of H_2 generation from AB hydrolysis. The catalytic activities for H_2 generation from AB hydrolysis are also investigated over various SP-ZSM-5-100 nanosheet-supported Rh-based bimetal catalysts at 298 K (Figure S38). On the basis of the Rh atoms, the TOF values of $Rh_{0.8}M_{0.2}$/SP-ZSM-5-100 (M = Cu, Mn, Ni, Fe, Co, Au, and Ru) are increased in turn, which are higher than that of monometallic Rh/SP-ZSM-5-100 (Figure 5e). Among all bimetallic catalysts, the $Rh_{0.8}Ru_{0.2}$/SP-ZSM-5-100 exhibits the highest TOF value of 1291 mol_{H2} mol_{Rh}^{-1} min^{-1}, indicating the synergistic effect of Rh−Ru is more conducive to improve the H_2 evolution rate from the hydrolysis of AB than that of other Rh-based bimetal species. Notably, the TOF value of $Rh_{0.8}Zn_{0.2}$/SP-ZSM-5-100 is slightly lower than that of Rh/SP-ZSM-5-100, indicating that the introduction of Zn cannot enhance the activity of Rh for AB hydrolysis.

Catalytic Activity of Cascade Hydrogenation of Nitroarenes by Coupling with the Hydrolysis of AB. The catalytic activity of Rh/Nano S-1, Rh/SP-S-1, Rh_1@S-1, and $Rh_{0.8}Ru_{0.2}$/SP-ZSM-5-100 catalysts for the cascade reactions that couples the hydrolysis of AB with the hydrogenation of nitrobenzene (0.2 mmol) and 4-nitroxylene (0.2 mmol) at 298 K are investigated. The catalytic results are shown in Figure 6 and Figures S39−S42 and Table 1. The nitrobenzene can be 100% converted to aniline (>99% selectivity) within 3 min over the Rh/SP-S-1, giving a high aniline generation rate of 133 $mol_{nitrobenzene}$ mol_{metal}^{-1} min^{-1}, which is 5- and 2-fold higher than that of Rh/Nano S-1 and Rh_1@S-1, respectively. The superior catalytic activity of Rh/SP-S-1 can be mainly attributed to the remarkably enhanced transport efficiency of reactants and products across the

https://dx.doi.org/10.1021/jacs.1c00578
J. Am. Chem. Soc. XXXX, XXX, XXX−XXX

ultrathin zeolite nanosheets. Significantly, thanks to the synergistic effect between bimetal components and Brønsted acid sites of zeolites, the aniline generation rate over $Rh_{0.8}Ru_{0.2}$/SP-ZSM-5-100 reaches up to 267 $mol_{nitrobenzene}$ mol_{metal}^{-1} min^{-1}, which represents the best activity among all previously reported heterogeneous catalysts under similar conditions.[13,45,46] By comparison, the nitrobenzene conversion is less than 1% after 20 min when the AB solution is replaced by the atmospheric H_2, and no product can be obtained without adding catalysts. The above results indicate that the in situ generated H_2 from AB hydrolysis in the catalytic system is much more efficient than the conventional gaseous H_2 for the reduction of the nitroarenes. The faster the H_2 generation rate from AB hydrolysis is, the higher the cascade nitrobenzene hydrogenation activity becomes. The catalytic activity of $Rh_{0.8}Ru_{0.2}$/SP-ZSM-5-100 for the cascade hydrogenation of nitrobenzene (1 mmol) in a higher concentration at 298 K is also investigated. As shown in Figure S43, the nitrobenzene in higher concentration can be 20% converted to aniline within 1 min over the $Rh_{0.8}Ru_{0.2}$/SP-ZSM-5-100 catalyst, giving a superhigh initial TOF value of 400 $mol_{nitrobenzene}$ mol_{metal}^{-1} min^{-1}. Significantly, the nitrobenzene can be 100% converted to aniline (>99% selectivity) within 8 min over the $Rh_{0.8}Ru_{0.2}$/SP-ZSM-5-100 catalyst, giving an aniline generation rate of 251 $mol_{nitrobenzene}$ mol_{metal}^{-1} min^{-1}.

Significantly, the 4-nitro-*o*-xylene with the larger molecular size can be also 100% converted to 3,4-dimethylaniline within 3 min over the $Rh_{0.8}Ru_{0.2}$/SP-ZSM-5-100, affording a high catalytic activity of 133 min^{-1}. However, no product can be obtained over Rh_1@S-1 because the molecular size of 4-nitro-*o*-xylene is larger than microporous sizes of **MFI** zeolite and fails to access the metal active sites inside the zeolites matrix. Most importantly, diverse nitroarenes, such as *p*-chloronitrobenzene, *p*-bromonitrobenzene, *p*-fluoronitrobenzene, 4-nitrotoluene, 3-nitrotoluene, and even bulky 1-nitronaphthalene can be totally converted to the corresponding amines (>99% selectivity) within 1.5−3 min catalyzed by $Rh_{0.8}Ru_{0.2}$/SP-ZSM-5-100 (Table 1 and Figures S44−S49). The above results indicate that the self-pillared zeolite nanosheet supported metal catalysts possess more extensive practicability and superior performance for cascade hydrogenation of different kinds of nitroarenes than previously reported nanosized zeolite-encaged metal catalysts and other heterogeneous catalysts.

CONCLUSION

In summary, we demonstrate that the self-pillared **MFI** zeolite nanosheets are powerful supports to immobilize various ultrasmall metallic clusters via a simple and industrially available impregnation method. As compared with conventional nanosized zeolite-supported metal catalysts, the self-pillared zeolite nanosheet-immobilized metal catalysts possessed remarkably decreased sizes of metal species, improved hydrophilicity and transport efficiency, and excellent thermal stability under diverse redox atmospheres at high temperatures. The as-prepared self-pillared zeolite nanosheet-supported metal catalysts are highly efficient in AB hydrolysis. Significantly, the optimized $Rh_{0.8}Ru_{0.2}$/SP-ZSM-5-100 exhibited a superhigh activity of H_2 generation rate from AB hydrolysis at 298 K, up to 1006 min^{-1}. Isotopic experiments reveal that both zeolite acidity and Rh−Ru synergy can promote the activation of water and significantly accelerate the H_2 generation from AB hydrolysis. The $Rh_{0.8}Ru_{0.2}$/SP-ZSM-5-100 also exhibited record catalytic activities in cascade hydrogenation of various nitroarenes by coupling with the hydrolysis of AB, which is even 4-fold higher than zeolite-encaged single-atom Rh catalysts due to its great superiority in fast transport of reactants and products during reactions. This work opens a new perspective for the utilization of ultrathin zeolite nanosheets as efficient supports to anchor ultrasmall metal nanocatalysts via simple and industrially available impregnation method. Most importantly, the zeolite nanosheet-supported metal catalysts exhibit excellent thermal stability under various atmospheres and significantly improved mass transfer efficiency across narrow micropores of zeolites, which can be expected to exhibit high performance in other important catalytic reactions. It should be pointed out that more kinds of small and stable metal species can also be expected to be immobilized in zeolite nanosheets via the impregnation method by taking into account solubilities, molecular sizes, and electrical properties of metal precursors.

ASSOCIATED CONTENT

Supporting Information

The Supporting Information is available free of charge at https://pubs.acs.org/doi/10.1021/jacs.1c00578.

Materials, methods, supporting figures, and tables (PDF)

AUTHOR INFORMATION

Corresponding Authors

Jihong Yu − *State Key Laboratory of Inorganic Synthesis and Preparative Chemistry, College of Chemistry and International Center of Future Science, Jilin University, Changchun 130012, People's Republic of China;* orcid.org/0000-0003-1615-5034; Email: jihong@jlu.edu.cn

Qiming Sun − *State Key Laboratory of Inorganic Synthesis and Preparative Chemistry, College of Chemistry, Jilin University, Changchun 130012, People's Republic of China; Innovation Center for Chemical Sciences, College of Chemistry, Chemical Engineering and Materials Science, Soochow University, Suzhou 215123, People's Republic of China;* orcid.org/0000-0002-8895-5703; Email: sunqiming@suda.edu.cn

Authors

Ning Wang − *State Key Laboratory of Inorganic Synthesis and Preparative Chemistry, College of Chemistry, Jilin University, Changchun 130012, People's Republic of China*

Tianjun Zhang − *State Key Laboratory of Inorganic Synthesis and Preparative Chemistry, College of Chemistry, Jilin University, Changchun 130012, People's Republic of China*

Alvaro Mayoral − *Center for High-resolution Electron Microscopy (CħEM), School of Physical Science and Technology, ShanghaiTech University, Shanghai 201210, People's Republic of China; Institute of Nanoscience and Materials of Aragon (INMA), Spanish National Research Council (CSIC), Advanced Microscopy Laboratory (LMA), University of Zaragoza, 50009 Zaragoza, Spain*

Lin Li − *Electron Microscopy Center, Jilin University, Changchun 130012, People's Republic of China*

Xue Zhou − *National Centre for Magnetic Resonance in Wuhan, State Key Laboratory of Magnetic Resonance and Atomic and Molecular Physics, Innovation Academy for*

https://dx.doi.org/10.1021/jacs.1c00578
J. Am. Chem. Soc. XXXX, XXX, XXX−XXX

Precision Measurement Science and Technology, Chinese Academy of Sciences, Wuhan 430071, People's Republic of China; orcid.org/0000-0002-6971-594X

Jun Xu − *National Centre for Magnetic Resonance in Wuhan, State Key Laboratory of Magnetic Resonance and Atomic and Molecular Physics, Innovation Academy for Precision Measurement Science and Technology, Chinese Academy of Sciences, Wuhan 430071, People's Republic of China*

Peng Zhang − *Department of Chemistry, Dalhousie University, Halifax, Nova Scotia B3H 4R2, Canada*

Complete contact information is available at: https://pubs.acs.org/10.1021/jacs.1c00578

Notes

The authors declare no competing financial interest.

■ ACKNOWLEDGMENTS

We thank the National Natural Science Foundation of China (Grants 21835002, 21920102005, and 21621001) and the 111 Project (B17020) for financial support. Q.S. acknowledges the Academic Start-up Funds of Soochow University (Q410901120). A.M. acknowledges The Centre for High-resolution Electron Microscopy (CℏEM), supported by SPST of ShanghaiTech University under contract. EM02161943; NFSC-21850410448 and to Spanish Ministry of Science under the Ramon y Cajal program (RYC2018-024561-I). This research used resources of the Advanced Photon Source, an Office of Science User Facility operated for the U.S. Department of Energy (DOE) Office of Science by Argonne National Laboratory, and was supported by the U.S. DOE under Contract No. DE-AC02-06CH11357, and the Canadian Light Source and its funding partners. We acknowledge Prof. Osamu Terasaki from ShanghaiTech University for his guidance and help in the C_s-corrected STEM measurements.

■ REFERENCES

(1) Liu, L.; Corma, A. Metal Catalysts for Heterogeneous Catalysis: From Single Atoms to Nanoclusters and Nanoparticles. *Chem. Rev.* **2018**, *118*, 4981−5079.

(2) Wang, N.; Sun, Q.; Yu, J. Ultrasmall Metal Nanoparticles Confined within Crystalline Nanoporous Materials: A Fascinating Class of Nanocatalysts. *Adv. Mater.* **2019**, *31*, 1803966.

(3) Flytzani-Stephanopoulos, M.; Gates, B. C. Atomically Dispersed Supported Metal Catalysts. *Annu. Rev. Chem. Biomol. Eng.* **2012**, *3*, 545−574.

(4) Farrusseng, D.; Tuel, A. Perspectives on zeolite-encapsulated metal nanoparticles and their applications in catalysis. *New J. Chem.* **2016**, *40*, 3933−3949.

(5) Chai, Y.; Shang, W.; Li, W.; Wu, G.; Dai, W.; Guan, N.; Li, L. Noble Metal Particles Confined in Zeolites: Synthesis, Characterization, and Applications. *Adv. Sci.* **2019**, *6*, 1900299.

(6) Wang, H.; Wang, L.; Xiao, F.-S. Metal@Zeolite Hybrid Materials for Catalysis. *ACS Cent. Sci.* **2020**, *6*, 1685−1697.

(7) Gates, B. C. Supported Metal Clusters: Synthesis, Structure, and Catalysis. *Chem. Rev.* **1995**, *95*, 511−522.

(8) Yang, X.-F.; Wang, A.; Qiao, B.; Li, J.; Liu, J.; Zhang, T. Single-Atom Catalysts: A New Frontier in Heterogeneous Catalysis. *Acc. Chem. Res.* **2013**, *46*, 1740−1748.

(9) Choi, M.; Wu, Z.; Iglesia, E. Mercaptosilane-Assisted Synthesis of Metal Clusters within Zeolites and Catalytic Consequences of Encapsulation. *J. Am. Chem. Soc.* **2010**, *132*, 9129−9137.

(10) Liu, L.; Díaz, U.; Arenal, R.; Agostini, G.; Concepción, P.; Corma, A. Generation of subnanometric platinum with high stability during transformation of a 2D zeolite into 3D. *Nat. Mater.* **2017**, *16*, 132−138.

(11) Wang, N.; Sun, Q.; Bai, R.; Li, X.; Guo, G.; Yu, J. In Situ Confinement of Ultrasmall Pd Clusters within Nanosized Silicalite-1 Zeolite for Highly Efficient Catalysis of Hydrogen Generation. *J. Am. Chem. Soc.* **2016**, *138*, 7484−7487.

(12) Sun, Q.; Wang, N.; Bing, Q.; Si, R.; Liu, J.; Bai, R.; Zhang, P.; Jia, M.; Yu, J. Subnanometric Hybrid Pd-M(OH)$_2$, M = Ni, Co, Clusters in Zeolites as Highly Efficient Nanocatalysts for Hydrogen Generation. *Chem.* **2017**, *3*, 477−493.

(13) Sun, Q.; Wang, N.; Zhang, T.; Bai, R.; Mayoral, A.; Zhang, P.; Zhang, Q.; Terasaki, O.; Yu, J. Zeolite-Encaged Single-Atom Rhodium Catalysts: Highly-Efficient Hydrogen Generation and Shape-Selective Tandem Hydrogenation of Nitroarenes. *Angew. Chem., Int. Ed.* **2019**, *58*, 18570−18576.

(14) Chai, Y.; Han, X.; Li, W.; Liu, S.; Yao, S.; Wang, C.; Shi, W.; da-Silva, I.; Manuel, P.; Cheng, Y.; Daemen, L. D.; Ramirez-Cuesta, A. J.; Tang, C. C.; Jiang, L.; Yang, S.; Guan, N.; Li, L. Control of Zeolite Pore Interior for Chemoselective Alkyne/Olefin Separations. *Science* **2020**, *368*, 1002−1006.

(15) Jin, Z.; Wang, L.; Zuidema, E.; Mondal, K.; Zhang, M.; Zhang, J.; Wang, C.; Meng, X.; Yang, H.; Mesters, C.; Xiao, F.-S. Hydrophobic Zeolite Modification for In Situ Peroxide Formation in Methane Oxidation to Methanol. *Science* **2020**, *367*, 193−197.

(16) Liu, Y.; Li, Z.; Yu, Q.; Chen, Y.; Chai, Z.; Zhao, G.; Liu, S.; Cheong, W.-C.; Pan, Y.; Zhang, Q.; Gu, L.; Zheng, L.; Wang, Y.; Lu, Y.; Wang, D.; Chen, C.; Peng, Q.; Liu, Y.; Liu, L.; Chen, J.; Li, Y. A General Strategy for Fabricating Isolated Single Metal Atomic Site Catalysts in Y Zeolite. *J. Am. Chem. Soc.* **2019**, *141*, 9305−9311.

(17) Cui, T.-L.; Ke, W.-Y.; Zhang, W.-B.; Wang, H.-H.; Li, X.-H.; Chen, J.-S. Encapsulating Palladium Nanoparticles Inside Mesoporous MFI Zeolite Nanocrystals for Shape-Selective Catalysis. *Angew. Chem., Int. Ed.* **2016**, *55*, 9178−9182.

(18) Wang, S.; Zhao, Z.-J.; Chang, X.; Zhao, J.; Tian, H.; Yang, C.; Li, M.; Fu, Q.; Mu, R.; Gong, J. Activation and Spillover of Hydrogen on Sub-1 nm Palladium Nanoclusters Confined within Sodalite Zeolite for the Semi-Hydrogenation of Alkynes. *Angew. Chem., Int. Ed.* **2019**, *58*, 7668−7672.

(19) Munnik, P.; de Jongh, P. E.; de Jong, K. P. Recent Developments in the Synthesis of Supported Catalysts. *Chem. Rev.* **2015**, *115*, 6687−6718.

(20) Zhang, X.; Liu, D.; Xu, D.; Asahina, S.; Cychosz, K. A.; Agrawal, K. V.; Al Wahedi, Y.; Bhan, A.; Al Hashimi, S.; Terasaki, O.; Thommes, M.; Tsapatsis, M. Synthesis of Self-Pillared Zeolite Nanosheets by Repetitive Branching. *Science* **2012**, *336*, 1684−1687.

(21) Han, J.; Cho, J.; Kim, J.-C.; Ryoo, R. Confinement of Supported Metal Catalysts at High Loading in the Mesopore Network of Hierarchical Zeolites, with Access via the Microporous Windows. *ACS Catal.* **2018**, *8*, 876−879.

(22) Choi, M.; Na, K.; Kim, J.; Sakamoto, Y.; Terasaki, O.; Ryoo, R. Stable Single-Unit-Cell Nanosheets of Zeolite MFI as Active and Long-Lived Catalysts. *Nature* **2009**, *461*, 246−249.

(23) Xu, D.; Ma, Y.; Jing, Z.; Han, L.; Singh, B.; Feng, J.; Shen, X.; Cao, F.; Oleynikov, P.; Sun, H.; Terasaki, O.; Che, S. π-π interaction of aromatic groups in amphiphilic molecules directing for single-crystalline mesostructured zeolite nanosheets. *Nat. Commun.* **2014**, *5*, 4262.

(24) Wang, J.; Liu, L.; Dong, X.; Alfilfil, L.; Hsiung, C.-E.; Liu, Z.; Han, Y. Converting Hierarchical to Bulk Structure: A Strategy for Encapsulating Metal Oxides and Noble Metals in Zeolites. *Chem. Mater.* **2018**, *30*, 6361−6369.

(25) Verheyen, E.; Jo, C.; Kurttepeli, M.; Vanbutsele, G.; Gobechiya, E.; Korányi, T. I.; Bals, S.; Van Tendeloo, G.; Ryoo, R.; Kirschhock, C. E. A.; Martens, J. A. Molecular Shape-Selectivity of MFI Zeolite Nanosheets in n-decane Isomerization and Hydrocracking. *J. Catal.* **2013**, *300*, 70−80.

(26) Kim, Y.; Kim, J.-C.; Jo, C.; Kim, T.-W.; Kim, C.-U.; Jeong, S.-Y.; Chae, H.-J. Structural and Physicochemical Effects of MFI Zeolite Nanosheets for the Selective Synthesis of Propylene from Methanol. *Microporous Mesoporous Mater.* **2016**, *222*, 1−8.

(27) Chaikittisilp, W.; Suzuki, Y.; Mukti, R. R.; Suzuki, T.; Sugita, K.; Itabashi, K.; Shimojima, A.; Okubo, T. Formation of Hierarchically Organized Zeolites by Sequential Intergrowth. *Angew. Chem., Int. Ed.* **2013**, *52*, 3355−3359.
(28) Sun, Q.; Wang, N.; Xu, Q.; Yu, J. Nanopore-Supported Metal Nanocatalysts for Efficient Hydrogen Generation from Liquid-Phase Chemical Hydrogen Storage Materials. *Adv. Mater.* **2020**, *32*, 2001818.
(29) Lang, C.; Jia, Y.; Yao, X. Recent Advances in Liquid-Phase Chemical Hydrogen Storage. *Energy Storag. Mater.* **2020**, *26*, 290−312.
(30) Zhan, W.-W.; Zhu, Q.-L.; Xu, Q. Dehydrogenation of Ammonia Borane by Metal Nanoparticle Catalysts. *ACS Catal.* **2016**, *6*, 6892−6905.
(31) Akbayrak, S.; Özkar, S. Ammonia Borane as Hydrogen Storage Materials. *Int. J. Hydrogen Energy* **2018**, *43*, 18592−18606.
(32) Heeribout, L.; Dorémieux-Morin, C.; Nogier, J. P.; Vincent, R.; Fraissard, J. Study of high-silica H-ZSM-5 acidity by ^{1}H NMR techniques using water as base. *Microporous Mesoporous Mater.* **1998**, *24*, 101−112.
(33) Xu, J.; Wang, Q.; Li, S.; Deng, F. Solid-State NMR in Zeolite Catalysis. *Lect. Notes Chem.* **2019**, *103*, 199−254.
(34) Xing, Y.; Wang, K.; Li, N.; Su, D.; Wong, W.-T.; Huang, B.; Guo, S. Ultrathin RuRh Alloy Nanosheets Enable High-Performance Lithium-CO_2 Battery. *Matter* **2020**, *2*, 1494−1508.
(35) Larichev, Y. V.; Netskina, O. V.; Komova, O. V.; Simagina, V. I. Comparative XPS Study of Rh/Al_2O_3 and Rh/TiO_2 as Catalysts for $NaBH_4$ Hydrolysis. *Int. J. Hydrogen Energy* **2010**, *35*, 6501−6507.
(36) Védrine, J. C.; Auroux, A.; Bolis, V.; Dejaifve, P.; Naccache, C.; Wierzchowski, P.; Derouane, E. G.; Nagy, J. B.; Gilson, J.-P.; van Hooff, J. H. C.; et al. Infrared, Microcalorimetric, and Electron Spin Resonance Investigations of the Acidic Properties of the H-ZSM-5 Zeolite. *J. Catal.* **1979**, *59*, 248−262.
(37) Jin, F.; Li, Y. A FTIR and TPD Examination of the Distributive Properties of Acid Sites on ZSM-5 Zeolite with Pyridine as a Probe Molecule. *Catal. Today* **2009**, *145*, 101−107.
(38) Sun, J.-K.; Zhan, W.-W.; Akita, T.; Xu, Q. Toward Homogenization of Heterogeneous Metal Nanoparticle Catalysts with Enhanced Catalytic Performance: Soluble Porous Organic Cage as a Stabilizer and Homogenizer. *J. Am. Chem. Soc.* **2015**, *137*, 7063−7066.
(39) Sun, J.-K.; Kochovski, Z.; Zhang, W.-Y.; Kirmse, H.; Lu, Y.; Antonietti, M.; Yuan, J. General Synthetic Route toward Highly Dispersed Metal Clusters Enabled by Poly(ionic liquid)s. *J. Am. Chem. Soc.* **2017**, *139*, 8971−8976.
(40) Luo, W.; Cheng, W.; Hu, M.; Wang, Q.; Cheng, X.; Zhang, Y.; Wang, Y.; Gao, D.; Bi, J.; Fan, G. Ultrahigh Catalytic Activity of l-Proline-Functionalized Rh Nanoparticles for Methanolysis of Ammonia Borane. *ChemSusChem* **2019**, *12*, 535−541.
(41) Xia, B. Q.; Liu, C.; Wu, H.; Luo, W.; Cheng, G. Z. Hydrolytic Dehydrogenation of ammonia borane catalyzed by metal-organic framework supported bimetallic RhNi nanoparticles. *Int. J. Hydrogen Energy* **2015**, *40*, 16391−16397.
(42) Fu, F. Y.; Wang, C. L.; Wang, Q.; Martinez-Villacorta, A. M.; Escobar, A.; Chong, H. B.; Wang, X.; Moya, S.; Salmon, L.; Fouquet, E.; Ruiz, J.; Astruc, D. Highly Selective and Sharp Volcano-type Synergistic Ni_2Pt@ZIF-8-Catalyzed Hydrogen Evolution from Ammonia Borane Hydrolysis. *J. Am. Chem. Soc.* **2018**, *140*, 10034−10042.
(43) Li, Z.; He, T.; Liu, L.; Chen, W.; Zhang, M.; Wu, G.; Chen, P. Covalent Triazine Framework Supported Non-Noble Metal Nanoparticles with Superior Activity for Catalytic Hydrolysis of Ammonia Borane: from Mechanistic Study to Catalyst Design. *Chem. Sci.* **2017**, *8*, 781−788.
(44) Chen, W.; Li, D.; Wang, Z.; Qian, G.; Sui, Z.; Duan, X.; Zhou, X.; Yeboah, I.; Chen, D. Reaction Mechanism and Kinetics for Hydrolytic Dehydrogenation of Ammonia Borane on a Pt/CNT Catalyst. *AIChE J.* **2017**, *63*, 60−65.
(45) Zhou, Y. H.; Yang, Q. H.; Chen, Y. Z.; Jiang, H. L. Low-cost CuNi@MIL-101 as an Excellent Catalyst toward Cascade Reaction: Integration of Ammonia Borane Dehydrogenation with Nitroarene Hydrogenation. *Chem. Commun.* **2017**, *53*, 12361−12364.
(46) Göksu, H.; Ho, S. F.; Metin, Ö.; Korkmaz, K.; Mendoza Garcia, A.; Gültekin, M. S.; Sun, S. Tandem Dehydrogenation of Ammonia Borane and Hydrogenation of Nitro/Nitrile Compounds Catalyzed by Graphene-Supported NiPd Alloy Nanoparticles. *ACS Catal.* **2014**, *4*, 1777−1782.

https://dx.doi.org/10.1021/jacs.1c00578
J. Am. Chem. Soc. XXXX, XXX, XXX−XXX